Journal of Materials Chemistry A



PAPER

View Article Online
View Journal | View Issue



Cite this: *J. Mater. Chem. A*, 2022, **10**, 7896

Syngas production at a near-unity H_2/CO ratio from photo-thermo-chemical dry reforming of methane on a Pt decorated $Al_2O_3-CeO_2$ catalyst[†]

Xuhui Feng,^a Zichen Du,^a Erik Sarnello,^b Wei Deng, ^{Da} Cullen R. Petru, ^{Da} Lingzhe Fang,^b Tao Li ^{Dbc} and Ying Li ^{D*a}

In this work, a Pt catalyst supported on an equimolar Al_2O_3 – CeO_2 binary oxide (Pt–Al–Ce) was prepared and applied in photo-thermo-chemical dry reforming of methane (DRM) driven by concentrated solar irradiation. It was found that the Pt–Al–Ce catalyst showed good stability in DRM reactions and significant enhancements in H_2 and CO production rates compared with Pt/CeO_2 (Pt–Ce) and Pt/Al_2O_3 (Pt–Al) catalysts. At a reaction temperature of 700 °C under 30-sun equivalent solar irradiation, the Pt–Al–Ce catalyst exhibits a stable DRM catalytic performance at a H_2 production rate of 657 mmol g^{-1} h^{-1} and a CO production rate of 666 mmol g^{-1} h^{-1} , with the H_2/CO ratio almost equal to unity. These production rates and the H_2/CO ratio were significantly higher than those obtained in the dark at the same temperature. The light irradiation was found to induce photocatalytic activities on Pt–Al–Ce and reduce the reaction activation energy. *In situ* diffuse reflectance infrared Fourier transform spectroscopy (*in situ* DRIFTS) was applied to identify the active intermediates in the photo-thermo-chemical DRM process, which were bidentate/monodentate carbonate, absorbed CO on Pt, and formate. The benefits of the binary Al_2O_3 – CeO_2 substrate could be ascribed to Al_2O_3 promoting methane dissociation while CeO_2 stabilized and eliminated possible coke formation, leading to high catalytic DRM activity and stability.

Received 25th November 2021 Accepted 20th February 2022

DOI: 10.1039/d1ta10088b

rsc.li/materials-a

1. Introduction

Synthesis gas, or syngas, a mixture of H₂ and CO, is an important material for a number of industrial applications as fuel gas or the raw material for varied chemical synthesis processes.¹ Currently, the most widely used technique for syngas production is the steam methane reforming (SMR) process,² where water vapor interacts with methane under high temperature and pressure conditions (700–1000 °C and 3–25 atm)³ and produces H₂ and CO. One of the drawbacks of the SMR process is the excessive amount of energy input required for water steam generation and reaction gas compression.²,³ Recent research progress has turned the spotlight on a milder syngas production technique, dry reforming of methane (DRM). The DRM process converts the two major greenhouse gases, CO₂ and CH₄, into syngas under atmospheric pressure in a relatively mild temperature range (650–850 °C),⁴ making it less energy-

demanding from the industrial application perspective. DRM

Recently, our research group introduced a photo-thermochemical approach for the DRM process, 14,15 where concentrated sunlight was applied to partially provide thermal energy and photoactive Pt/CeO₂-based catalysts (Pt decorated Sidoped 14 and Zn-doped CeO₂ 15) were used to make better use of the concentrated sunlight and further improve the DRM performance. The Pt–CeO₂-based catalysts show highly efficient and stable DRM catalyzing capabilities and exhibit substantial DRM reaction rate enhancements under concentrated sunlight irradiation, compared to those under dark conditions. The Pt–CeO₂-based catalysts convert photon energy into chemical energy through photo-induced activities on the metal oxide substrate. 14,16,17 The high performance and stability of the

has been suggested as an environmental strategy to utilize $\rm CO_2$ molecules for valuable chemical/fuel production. ^{5,6} In addition, DRM makes it possible to directly use the $\rm CO_2$ impurities that already exist in natural gas, ⁷ which is particularly favorable for oil field gas that contains a significant concentration of $\rm CO_2$. The ideal $\rm H_2$: $\rm CO$ ratio of DRM syngas is 1:1, which fits an industrial hydroformylation process. ⁸ Despite the advantages of DRM and the reduced energy consumption compared with SMR, a relatively high temperature is still needed to initiate the traditional thermal-driven DRM process, ⁹⁻¹¹ which, again, demands extensive energy input. ^{12,13} Further innovations to lower the energy demand are necessary.

^aJ. Mike Walker '66 Department of Mechanical Engineering, Texas A&M University, College Station, TX 77843, USA. E-mail: yingli@tamu.edu

^bDepartment of Chemistry and Biochemistry, Northern Illinois University, DeKalb, IL 60115, USA

^cX-ray Science Division, Advanced Photon Source, Argonne National Laboratory, Lemont, IL 60439, USA

[†] Electronic supplementary information (ESI) available. See DOI: 10.1039/d1ta10088b

Paper

photo-thermal driven DRM reaction on Pt–CeO₂-based catalysts benefit from both the photoactivity¹⁶ and the high surface oxygen mobility¹⁸ of the CeO₂ substrate, which also promotes the coke resistance capacity of the catalysts.

In addition to the high energy consumption, another issue involved in the DRM process is the H₂/CO ratio that is lower than 1.0 in the products, which is likely related to a side reaction: reverse water-gas shift (RWGS) reaction $(H_2 + CO_2 \rightarrow H_2O)$ + CO). 19,20 The DRM process on a number of noble metal-based catalytic materials, including Ru-based,21,22 Pt-based,15,23 Rhbased,24 and Pd-based25,26 catalysts, shows deteriorated H2/CO ratios. For example, Damyanova et al.27 applied a type of Pt/ CeO₂-ZrO₂ catalyst for the DRM reaction; only a low H₂/CO ratio of 0.51 was observed, which is likely associated with the presence of basic centers on the ZrO2 material.28 Wysocka et al.29 studied and compared the DRM performance of Ru-Ni/ZrO2 and Ru-Ni/Al₂O₃ catalysts. However, due to the tendency of the Ru catalyst in promoting RWGS reactions,30 only a H2/CO ratio of \sim 0.7 was obtained. Advanced catalyst design is demanded to improve H₂ selectivity in the DRM process.

In efforts to design high H₂/CO ratio generation catalysts, Benrabaa et al.31 recently reported the application of SiO₂ supported nickel ferrite catalysts in the DRM process, where it was demonstrated that the H₂/CO production ratio can be promoted by Lewis acidic sites on the catalyst surface. However, Hambali et al.32 later indicated that strong catalyst surface acidity may lead to, despite enhanced H2 selectivity, catalyst coking and deactivation. In light of these two studies, it seems that an improved H₂/CO ratio can be achieved by coupling a catalyst with a weak acidic promoter. In this sense, Al₂O₃, a type of abundant and low-cost chemical compound with intrinsic mild acidic characteristics33,34 that has long been in catalyst design in a number of industrial processes including hydrocarbon isomerization,34 catalytic cracking,35 etc., can be an ideal addition on DRM catalysts to improve hydrogen production selectivity in the DRM process.

In this work, a Pt decorated equimolar Al₂O₃-CeO₂ catalyst was prepared and applied for the photo-thermal driven DRM process. The first objective of this study is to introduce a facile and economic approach to catalyst design to improve the catalytic activity and H₂/CO ratio in the DRM process. Based on the aforementioned literature review, it is expected that the Pt/ Al₂O₃-CeO₂ material promotes H₂ generation and enhances the H₂/CO ratio in the DRM process catalyzed compared with the Pt-CeO₂ based catalyst. Additionally, although alumina has been long applied as a substrate material in the DRM process,36,37 there are still knowledge gaps regarding the synergetic effects between Al₂O₃ and CeO₂ in photo-driven DRM processes. Therefore, more importantly, the second objective of this work is to investigate the synergetic effects of Al₂O₃ and CeO₂ as substrates in photo-driven DRM processes. Thirdly, although a number of studies14,15,38-41 have demonstrated that light irradiation promotes DRM performance on photoactive catalysts, the mechanism behind the performance enhancement is still not fully understood. For this reason, the third objective of this work is to uncover the role of light irradiation in the photo-thermo-chemical DRM process.

Experimental

2.1 Catalyst preparation

Metal oxide substrates were prepared according to previous reports14,15 with minor modifications. To prepare the CeO₂ substrate, two solutions were made. Solution A was prepared by dissolving 5 mmol cetyl trimethyl ammonium bromide (CTAB, C₁₉H₄₂NBr, high purity, VWR) in 7.9 g reagent alcohol (>96% ethanol, VWR). Solution B was made by mixing 5 mmol cerium nitrate hexahydrate [Ce(NO₃)₃·6H₂O, 99.99%, BTC] and 5 mmol citric acid ($C_6H_8O_7$, 99.5+%, Alfa Aesar) in 7.9 g reagent alcohol. Solutions A and B were then mixed and stirred for 3 h before being placed in an oven maintained at 60 °C overnight to allow the solvent to evaporate. The solidified gel was then calcined in air at 500 °C for 5 h. The Al₂O₃ substrate was prepared by using 5 mmol aluminum nitrate nonahydrate $[Al(NO_3)_3 \cdot 9H_2O_1] \ge 98\%$, Sigma Aldrich] instead of cerium nitrate hexahydrate to prepare solution B. The Al₂O₃-CeO₂ hybrid substrate was prepared by using 5 mmol Al(NO₃)₃·9H₂O and 5 mmol Ce(NO₃)₃·6H₂O (nominal atomic ratio Al: Ce = 1:1) instead of solely $Ce(NO_3)_3 \cdot 6H_2O$ or $Al(NO_3)_3 \cdot 9H_2O$ to prepare solution B.

A wet impregnation method was applied to deposit 1 wt% Pt on the metal oxide substrates and prepare the DRM catalysts. 100 mg metal oxide substrate was dispersed in a liquid mixture containing 5 g deionized water, 4 g methanol (CH₄O, >99.98%, VWR), 4 g acetone (C₃H₆O, VWR), and 2.1 mg chloroplatinic acid (H₂PtCl₆, 99.9%, Alfa Aesar, equivalent to 1 mg Pt) in an alumina crucible. The crucible was then placed on a hot plate maintained at 100 °C, and the suspension was stirred with a magnetic bar to allow the solvent to evaporate. After the evaporation, the solid was collected and calcined in air at 500 °C for 2 h. The materials prepared with the CeO₂ substrate, Al₂O₃ substrate, and Al₂O₃–CeO₂ hybrid substrate are denoted as Pt–Ce, Pt–Al, and Pt–Al–Ce, respectively.

2.2 Catalyst characterization

X-ray diffraction (XRD) patterns were obtained on a Bruker-AXS D8 advanced Bragg-Brentano X-ray powder diffractometer. Energy-dispersive X-ray spectroscopy (EDS) analysis was conducted with a JEOL JSM-7500F field emission scanning electron microscope (FE-SEM). The morphology of catalyst samples was investigated on a JEOL JEM2100F transmission electron microscope (TEM). X-ray photoelectron spectroscopy analyses were conducted on an Omicron DAR 400 XPS/UPS system. UV-Vis light absorption data were obtained on a Hitachi U-4100 UV-Vis-NIR spectrophotometer.

2.3 Photo-thermal driven DRM performance measurements

The experimental setup of the photo-thermal driven DRM catalyst performance measurements is similar to that employed in our previous studies. As shown in Fig. S1,† a Science Tech solar simulator (operated at 1200 W, equivalent to 30-sun irradiation; the light spectrum is shown in Fig. S2†) was used as the light source. A 5 mg catalyst sample was dispersed in 2 ml deionized water to form a catalyst suspension. The suspension was then dripped onto a piece of oval-shaped quartz fiber paper,

which was later placed onto an oval catalyst holder. The catalyst holder was then placed into a quartz tube reactor (Fig. S1†). The position of the catalyst holder was carefully aligned inside the reactor to ensure that the thermocouple tip comes into contact with the quartz filter surface and aligns with the centerline of the catalyst holder and the reactor. The tube reactor was heated in a tube furnace, where a window was made to allow sunlight to irradiate on the catalyst. Prior to the performance test, the catalyst was firstly reduced at 700 °C with a gas mixture of H₂ (20.2 standard cubic centimeter per minute, or 20.2 sccm) and Ar (43.6 sccm) for 1 h, while two mass flow controllers controlled the gas flow rates. After the reduction process, the furnace was powered off, and the tube reactor was then purged with Ar (150 sccm) to eliminate H_2 in the reactor. After 30 min of Ar purging, the solar simulator was powered on at 1200 W and the tube furnace was turned on and set at a desired reaction temperature while maintaining the Ar gas flow. The solar lamp operated at 1200 W alone can only heat up the reactor to \sim 450 °C. Therefore, auxiliary heating from the furnace is needed. Once the reactor reached the desired reaction temperature, the Ar gas flow was turned off and a premixed gas mixture (10% CH₄, 10% CO₂, and balanced Ar, hereinafter referred to as "reaction gas") was introduced into the reactor at a gas flow rate of 12 sccm. The outlet of the reactor is connected to a Shimadzu GC-2014 gas chromatograph to determine the chemical composition of the produced gas. Similar tests were conducted without concentrated solar irradiation.

2.4 *In situ* diffuse reflectance infrared Fourier transform spectroscopy (*in situ* DRIFTS) analyses

A similar setup reported in our previous study was applied to conduct the *in situ* DRIFTS analyses. 42 The data acquisition was performed with a Nicolet 6700 spectrometer (Thermo Electron) equipped with a Praying Mantis DRIFTS accessory and a reaction chamber (Harrick Scientific, HVC-DRP). Fig. S3† shows the diagram of the in situ DRIFTS reaction chamber. The highest temperature the reaction chamber can reach is 600 °C. Prior to each in situ DRIFTS test, the catalyst sample was firstly reduced with a gas mixture of H₂ (20.2 sccm) and Ar (43.6 sccm) for 15 min at 600 °C in the DRIFTS reaction chamber. After the reduction process, the H2 gas flow was turned off and the reaction chamber was allowed to cool down naturally to the target testing temperature, while Ar protected the catalyst sample at a flow rate of 43.6 sccm. Once the DRIFT chamber reached the target temperature, the FTIR background was then taken, followed by introducing the same reaction gas used in the DRM performance test at 12 sccm. The catalyst sample was then allowed to interact with the reaction gas (under a continuous flow), while multiple DRIFTS data were taken and recorded under dark conditions over the next 10 min. It normally takes \sim 3 min for the catalyst surface to get saturated with the reaction gas. Therefore, 10 min is adequate for the catalyst to reach the adsorption equilibrium. After the dark equilibrium DRIFTS spectra were taken, concentrated sunlight was then applied to the sample through the quartz window. The same solar lamp used in the DRM performance test was applied as the light source, and the power of the lamp was set at 1200 W. An optical fiber was used to direct the light into the DRIFTS reaction chamber. The intensity of the light exiting the optical fiber was measured to be close to 1 sun, and the light spectrum is shown in Fig. S4.† Immediately after the concentrated sunlight was applied to the DRIFTS cell, another set of DRIFTS data acquisition was conducted. Multiple DRIFTS data were taken and recorded over the next 5 minutes, which is adequate for the catalyst to reach new absorption equilibrium under solar irradiation (normally takes less than 1 min). Similar *in situ* DRIFTS analyses were also performed with a $CO_2: Ar = 10: 90$ gas mixture and a $CH_4: Ar = 10: 90$ gas mixture.

3. Results and discussion

3.1 Crystal structure

The XRD patterns of Pt-Ce, Pt-Al-Ce, and Pt-Al are displayed in Fig. 1. The characteristic XRD pattern of CeO2 was found on both Pt-Ce and Pt-Al-Ce, while the characteristic peaks of Pt were not found in the XRD patterns of either sample. The Pt nanoparticles are likely tiny and well distributed on the surface of Pt-Ce and Pt-Al-Ce. By comparing the XRD patterns of Pt-Ce and Pt-Al-Ce, it was noted that the XRD peaks of Pt-Al-Ce are broadened. This observation is likely related to the decreased CeO₂ crystallite size due to the combination of CeO₂ and Al₂O₃. The XRD pattern of Pt-Al indicates that the phase of the Al₂O₃ support is γ -Al₂O₃, and the elementary Pt [111] peak was found at $2\theta = \sim 39.7^{\circ}$, which confirms the existence of Pt in the Pt-Al catalyst. Since the weight percentage of Pt is the same in all of the three catalysts, the observation of Pt [111] in Pt-Al suggests that the size of Pt nanoparticles is significantly larger than that on Pt-Ce and Pt-Al-Ce.

Interestingly, no characteristic peaks of γ -Al₂O₃ were found in the XRD pattern of Pt–Al–Ce, and similar results were also previously observed in several studies on Al₂O₃–CeO₂ hybrid metal oxide materials.^{43–45} This is likely related to the low crystallinity of the γ -Al₂O₃ substrate, as evidenced by the wide and

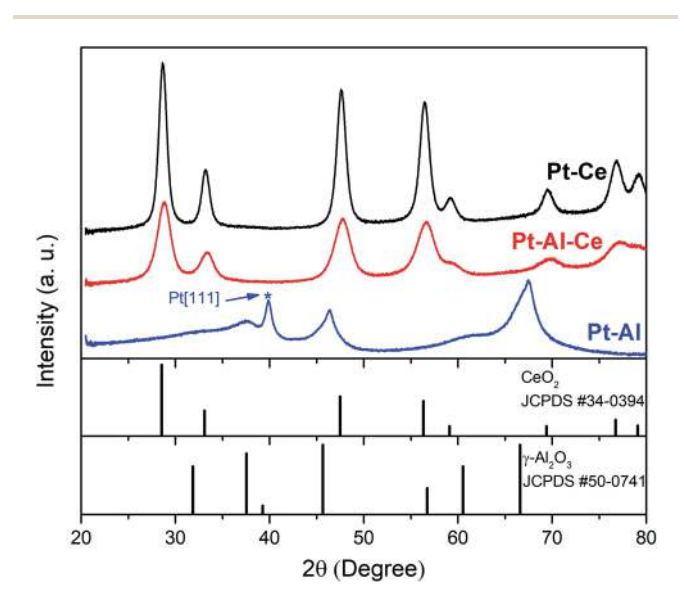


Fig. 1 XRD patterns of Pt-Ce, Pt-Al and Pt-Al-Ce.

less-defined peaks in the XRD pattern of Pt–Al. Since the CeO_2 phase in Pt–Ce shows sharp and well-defined peaks, it is likely that in Pt–Al–Ce, the highly crystallized CeO_2 peaks overshadow those of γ -Al₂O₃, resulting in the absence of γ -Al₂O₃ peaks.

3.2 Morphology

Fig. 2 shows the TEM images of Pt-Ce, Pt-Al-Ce, and Pt-Al. As shown in Fig. 2a, the particle size of the Pt decorated CeO₂ catalyst is \sim 20 nm, and the catalyst particles show sharp edges and corners. Pt-Al-Ce material particles show a diameter of \sim 15 nm (Fig. 2c) and the particles are oval-shaped. Different from Pt-Ce and Pt-Al-Ce, the particle size of Pt-Al is significantly larger. As shown in Fig. 2e, the particle size distribution of Pt-Al ranges from ~100 nm to several hundred nanometers. CeO₂ [111] (0.31 nm) and CeO₂ [100] (0.27 nm) were noted in Pt-Ce and Pt-Al-Ce, according to Fig. 2b and d, which coincide with the XRD results. As shown in the CeO₂ lattice in Fig. 2b, the CeO₂ phase in the Pt–Ce material shows long-range order, while the CeO₂ phase in Pt-Al-Ce only exhibits short-range order (Fig. 2d). It seems that the Al₂O₃ phase breaks down the longrange order of crystalline CeO₂ in Pt-Al-Ce, which verifies that the phases of Al₂O₃ and CeO₂ are segregated phases instead of a solid solution form. Pt [111] (0.21 nm) spacing was found in Pt-Ce, Pt-Al-Ce, and Pt-Al, confirming the existence of Pt. The sizes of Pt nanoparticles on Pt-Ce, Pt-Al-Ce, and Pt-Al were measured with ImageJ based on a number of TEM images. The average Pt particle size on Pt-Ce, Pt-Al-Ce, and Pt-Al was calculated to be 1.9 nm, 1.4 nm, and 6.8 nm, respectively. The histograms of Pt nanoparticle sizes on the three catalysts are included in Fig. S5.† The Pt nanoparticle sizes on Pt-Al are significantly greater than those on Pt-Ce and Pt-Al-Ce. The

large size of Pt nanoparticles coincides with the XRD pattern of Pt-Al, where the Pt [111] peak is prominent.

To confirm the existence of the Al element in Pt–Al–Ce, elemental mapping was performed by energy-dispersive X-ray spectroscopy (EDS). The EDS result is included in the ESI as Fig. S6.† The elemental mapping of Pt–Al–Ce shows strong signals of Ce and Al, confirming that Ce and Al are the major elements in Pt–Al–Ce. Pt was also found in the EDS mapping, while the Pt signal is much weaker compared to those of Ce and Al, which is reasonable due to the low concentration of Pt (1.0 wt%) in Pt–Al–Ce.

3.3 Surface chemical properties

X-ray photoelectron spectroscopy (XPS) analysis of the Ce 3d orbital was conducted on Pt-Ce and Pt-Al-Ce to investigate the effect of Al₂O₃-CeO₂ incorporation on the chemical states of CeO₂. Prior to the XPS testing, the catalysts were pre-reduced in an Ar/H₂ gas mixture as they would be in DRM performance tests. XPS analyses of Pt or Al were not performed as the XPS binding energies of the two elements overlap, making it impractical to reach meaningful results or conclusions. The existence of Ce³⁺ in the catalyst surface indicates the formation of oxygen vacancies, likely generated during the H2 reduction process. The oxygen vacancy has been deemed a key factor for achieving high DRM performance. 15,46 As shown in Fig. 3, the Ce 3d spectra can be well deconvoluted into Ce^{4+} and Ce^{3+} , where v_o , v', u_o , and u' correspond to Ce³⁺; v, v", v"', u, u", and u"' correspond to Ce⁴⁺. 15,47-49 Based on the Ce 3d deconvolution results, the molar ratios of Ce³⁺/ $(Ce^{3+} + Ce^{4+})$ on Pt–Ce and Pt–Al–Ce are calculated to be 24.3% and 24.7%, respectively. It seems that the incorporation of Al₂O₃ into Pt-CeO₂ does not significantly promote the formation of Ce³⁺. The

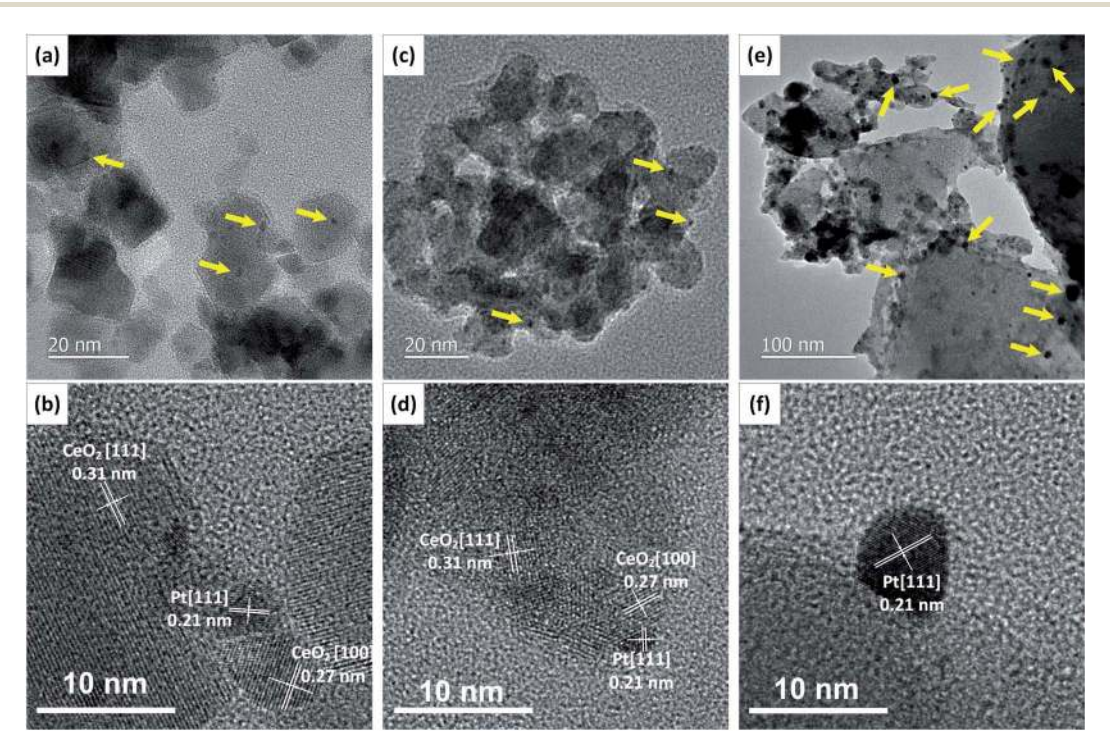


Fig. 2 TEM images of Pt-Ce (a & b), Pt-Al-Ce (c & d), and Pt-Al (e & f); yellow arrows point to Pt nanoparticles.

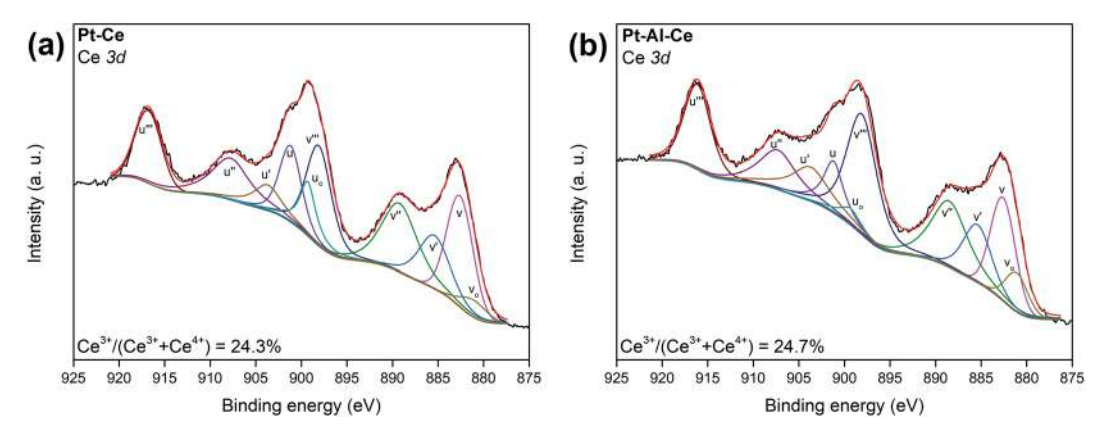


Fig. 3 Deconvolution of Ce 3d XPS spectra of Pt-Ce and Pt-Al-Ce catalysts.

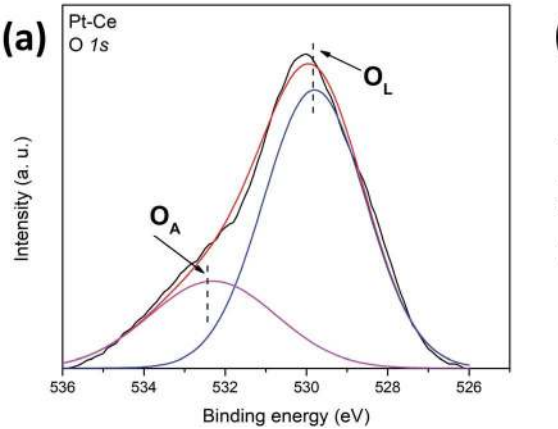
 ${\rm Ce}^{3^+}/({\rm Ce}^{3^+}+{\rm Ce}^{4^+})$ values on both of the catalysts are similar; however, considering the incorporation of a high concentration of ${\rm Al}_2{\rm O}_3$ in Pt–Al–Ce, the oxygen vacancy concentration on Pt–Al–Ce can be significantly lower than that on Pt–Ce.

To better compare the surface oxygen vacancy concentrations between Pt-Ce and Pt-Al-Ce, the deconvolution of O 1s was also performed. The difference in the binding energy values of the lattice oxygen (O_L) on Al₂O₃ and CeO₂ was found to be very close to each other.50-53 Therefore, the two types of lattice oxygen atoms were considered as a whole, whose peak is located at \sim 529.9 eV. The peak at \sim 532.0 eV was identified as adsorbed oxygen (OA) on oxygen vacancies, which can be applied to determine the concentration of surface vacancies. 50,51,54 Based on the O 1s deconvolution result shown in Fig. 4, the OA concentrations on Pt-Ce and Pt-Al-Ce were calculated to be 27.0% and 15.5%, respectively. Compared with Pt-Ce, Pt-Al-Ce exhibits a relatively lower concentration of oxygen vacancies, which is reasonable as only CeO₂ is able to produce oxygen vacancies in a reducing environment and CeO2 is diluted due to the existence of Al₂O₃ in Pt-Al-Ce.

3.4 Optical properties

To investigate the optical properties and calculate the bandgaps of the as-prepared catalysts, UV-Vis diffuse reflectance spectra and bandgap analyses were performed. As shown in Fig. 5a, Pt–Ce absorbs light mainly in the wavelength range below 400 nm, showing two major absorption bands located at 250 nm and 351 nm, in agreement with the CeO₂ light absorption properties reported in a previous study. FP-Al-Ce also shows a major absorption of photons with a shorter wavelength than 400 nm, while the absorption band at $\sim\!\!250$ nm shows a slight intensity decline. Different from Pt-Ce and Pt-Al-Ce, Pt-Al only shows absorption at $\sim\!\!258$ nm, which is identified as the light absorption of alumina. The light absorption of Pt nanoparticles likely causes the light absorption in the visible light range.

Bandgap analysis was performed with the Tauc plot based on the procedure reported by Makula *et al.* previously.⁵⁷ Fig. 5b shows the bandgap analyses of Pt–Ce, Pt–Al–Ce, and Pt–Al. The bandgaps of Pt–Ce and Pt–Al–Ce were calculated to be 2.3 eV and 2.4 eV, respectively. The Pt–Al–Ce material only shows a bandgap value change of 0.1 eV; it seems that the existence Al₂O₃ does not cause a significant bandgap variation on the CeO₂ component in Pt–Al–Ce. However, according to the Tauc plot of Pt–Al, it is not plausible to determine the bandgap value of Pt–Al. This result suggests that the Pt–Al catalyst is not photoactive. The obtained bandgap value of Pt–Ce is lower compared with the calculated values in our previously reported values.^{14,15} As mentioned, the catalysts were reduced prior to the



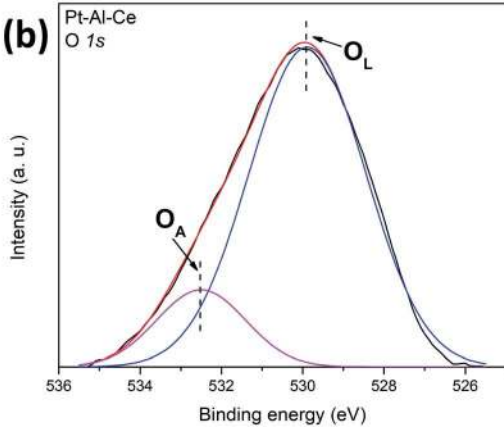
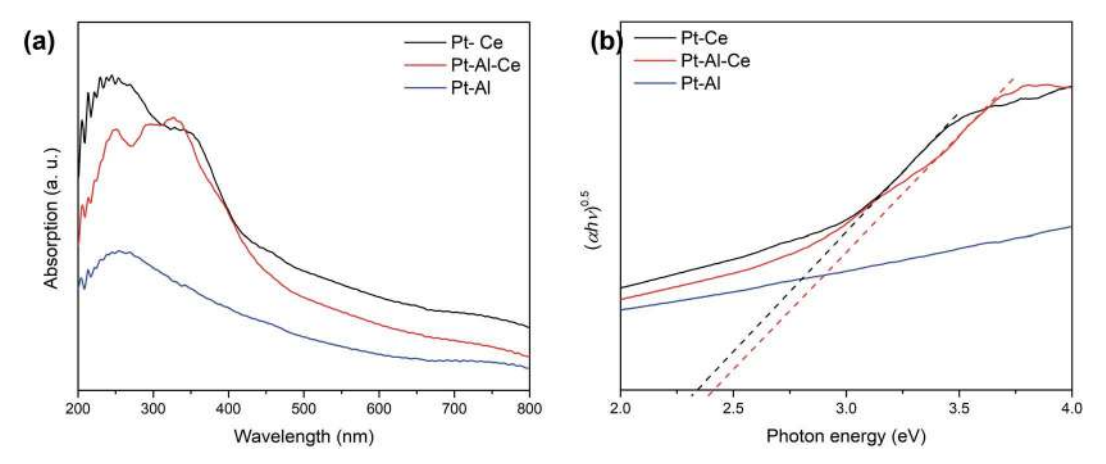
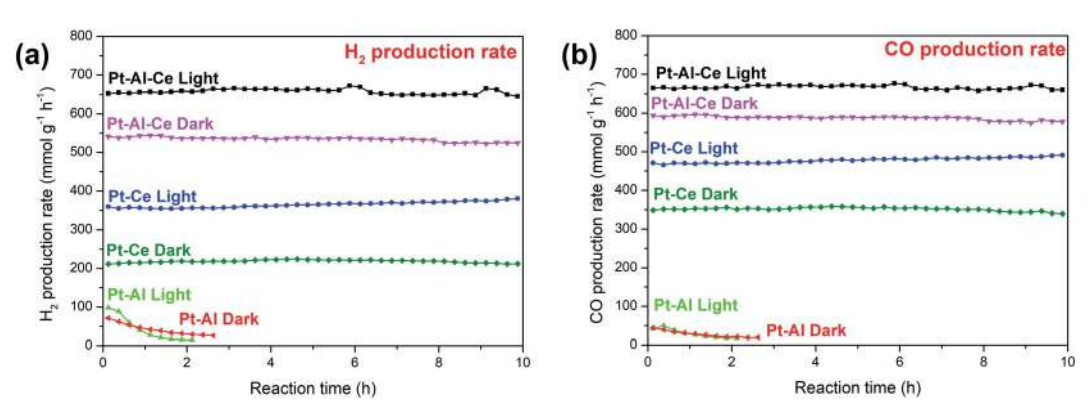


Fig. 4 Deconvolution of O 1s XPS spectra of Pt-Ce and Pt-Al-Ce catalysts.



UV-Vis light absorption spectra (a) and Tauc plots (b) of Pt-Ce, Pt-Al-Ce, and Pt-Al materials.



DRM performance: (a) H₂ production and (b) CO production of Pt-Ce, Pt-Al and Pt-Al-Ce at 700 °C under light and dark conditions.

UV-Vis diffuse reflectance measurements. The oxygen vacancy generated from the reduction process is likely responsible for the narrowed bandgaps of Pt-Ce and Pt-Al-Ce. 58,59

3.5 DRM performance

The DRM performance data of Pt-Al-Ce, Pt-Ce, and Pt-Al at 700 °C under both dark conditions and concentrated sunlight are presented in Fig. 6. The three catalysts show structural and morphological stability after the experiments, as shown in Fig. S7 and S8.† The numerical results of the DRM performance are listed in Table 1, where the listed values are the averages of all DRM performance data presented in Fig. 6. Both Pt-Ce and Pt-Al-Ce showed good stability under both dark and light conditions for the DRM process at 700 °C. Both catalysts showed DRM performance enhancement under light conditions compared with those under dark conditions, as shown in Fig. 6. Notably, under concentrated solar irradiation, Pt-Al-Ce delivered a near-unity H2/CO production ratio of 0.99, which is significantly improved compared with that of Pt-Ce (0.77 under light conditions).

In contrast, Pt-Al deactivates fast under both reaction conditions within less than 2 h in the DRM process. No significant difference in DRM performance was observed

related to solar irradiation. Al₂O₃ is not considered photoactive. It is, therefore, reasonable that the concentrated sunlight does not make a significant difference in the DRM performance of the Pt-Al catalyst. Regarding the DRM catalyzing stability of Pt-Al, as previously reported by Hambali et al., 32 a DRM catalyst with an over-acidic surface may result in deactivation in the DRM process due to coke accumulation. Although Al₂O₃ is a type of material that shows only weak surface acidity under

Table 1 DRM performance of Pt-Ce, Pt-Al-Ce and Pt-Al at 700 °C (average of data in Fig. 6)

Sample ID	H_2 production rate (mmol $g^{-1} h^{-1}$)	CO production rate $(\text{mmol g}^{-1} \text{ h}^{-1})$	H ₂ /CO ratio
Under dark o	conditions		
Pt-Ce	218	351	0.62
Pt-Al-Ce	535	588	0.91
Pt-Al	42	28	1.50
Under solar	irradiation		
Pt-Ce	365	477	0.77
Pt-Al-Ce	657	666	0.99
Pt-Al	43	30	1.44

DRM reaction conditions,³³ it seems that the surface acidity of the pure Al_2O_3 support is already too high for the DRM process to maintain a stable catalytic activity. As shown in Table 1, the H_2/CO ratios on Pt–Al under light and dark conditions were calculated to be 1.50 and 1.44, respectively. A value of the H_2/CO ratio higher than 1.0 in the DRM process suggests a higher methane dissociation rate than the coke carbon gasification rate, which leads to coke accumulation and causes performance deactivation.

As determined by the TEM analyses, there is a difference between the size of Pt nanoparticles on Pt-Ce (1.9 nm) and Pt-Al-Ce (1.4 nm). The size of Pt nanoparticles deposited on the catalysts is a crucial factor in determining the DRM reaction rate. However, little information was found in the literature on the effect of Pt nanoparticle sizes on the reaction rate of DRM reactions. In a similar material system, however, Gascon et al. 60 investigated the effect of rhodium (Rh) particle size on DRM reaction rates, where Rh nanoparticles were deposited on three substrates, namely CeO2, CeO2-ZrO2, and ZrO2. It was found that the DRM reaction rates on the catalysts showed a linear correlation with the Rh nanoparticle size in the range of 1.6-8.0 nm. This study applied a similar catalyst system and conducted the same reaction process as in the present work. More importantly, as a type of noble metal, Rh nanoparticles promote the DRM reaction rate in a similar way to Pt. Based on the work of Gascon et al., given the fact that Rh is generally more active as an active species than Pt in the DRM process,61 the small difference in Pt nanoparticle sizes between Pt-Ce and Pt-Al-Ce is unlikely to make a significant difference in the DRM reaction rates on Pt-Ce and Pt-Al-Ce.

An apparent synergistic effect of Al₂O₃ and CeO₂ as catalyst supports is observed on Pt-Al-Ce. Pt-Al-Ce considerably outperforms both Pt-Ce and Pt-Al in H2 and CO production rates. Compared with Pt-Ce, Pt-Al-Ce shows significant enhancement in CO and H2 production rates under both light and dark conditions (67.2% and 144.8% enhancements in CO and H₂ in the dark, respectively; 39.6% and 80.0% improvements in CO and H₂ under light, respectively). Compared with Pt-Al, Pt Al-Ce exhibits good stability, in addition to the notably promoted H₂ and CO production rates. The significant improvement in the H₂ generation rate on Pt-Al-Ce suggests that methane dissociation was strongly promoted. In this sense, the incorporation of Al₂O₃ into CeO₂ is advantageous due to the high efficiency of CeO2 in the oxidation of surface deposited coke to CO.^{27,62,63} In this regard, in the Pt-Al-Ce material, the Al₂O₃-CeO₂ support is likely bi-functional: firstly, Al₂O₃ promotes methane dissociation on Pt nanoparticles, resulting in improved H2 generation; secondly, CeO2 acts as a catalyst performance stabilizer by eliminating any possible coke formed from methane dissociation. It is likely that the two possible mechanisms work jointly to promote the DRM performance on the Pt-Al-Ce catalyst.

To confirm the above hypotheses and further investigate the synergistic effect of Al_2O_3 and CeO_2 on the Al_2O_3 – CeO_2 binary substrate, a CeO_2 -rich Pt–Al–Ce catalyst (Al : Ce molar ratio = 2:10, denoted as Ce-Rich-PAC) and an Al_2O_3 -rich Pt–Al–Ce catalyst (Al : Ce molar ratio = 10:2, denoted as Al-Rich-PAC)

were prepared and tested for DRM performance under solar irradiation at 700 °C, and the results are shown in Fig. S9.† Ce-Rich-PAC shows stable catalytic activities, and the 10 h average of CO and H₂ production rates of Ce-Rich-PAC are 602 mmol g⁻¹ h⁻¹ and 549 mmol g⁻¹ h⁻¹, respectively. Even with a low Al₂O₃ incorporation concentration in the catalyst, Ce-Rich-PAC shows notable enhancements in catalytic performance than those of Pt-Ce. The H₂/CO production ratio of Ce-Rich-PAC was 0.91, considerably higher than that of Pt-Ce and only slightly lower than that of Pt-Al-Ce. In contrast to the stable DRM performance of Ce-Rich-PAC, Al-Rich-PAC shows a deteriorating catalytic performance over time: the initial CO and H2 production rates are 641 mmol g^{-1} h^{-1} and 728 mmol g^{-1} h^{-1} , respectively, which dropped to 581 mmol $g^{-1} h^{-1}$ and 596 mmol g⁻¹ h⁻¹ after 10 h, respectively. Interestingly, the initial CO production rate on Al-Rich-PAC is slightly lower than that of Pt-Al-Ce, but the initial H₂ production rate on Al-Rich-PAC is \sim 9% higher than that of Pt-Al-Ce. This result again implies that Al₂O₃ promotes H₂ generation from methane dissociation. In the 10 h test, the H₂/CO production ratio on Al-Rich-PAC is always greater than 1.0, suggesting a higher methane dissociation reaction rate and coke accumulation on the catalyst, which leads to deactivation of DRM performance. Despite the DRM catalytic deactivation of Al-Rich-PAC over time, compared with Pt-Al, Al-Rich-PAC exhibits remarkable improvements in both catalytic performance and stability, even with a low CeO₂ incorporation concentration. The enhancements are likely related to the superior coke gasification ability of CeO₂, which minimizes coke accumulation and preserves the activity of the catalyst. 64 However, with a low CeO2 incorporation amount, Al-Rich-PAC still shows deterioration in catalytic performance over time.

To determine the effect of Pt concentration of the Pt–Al–Ce catalyst on the DRM process, varied amounts of Pt (0.25 wt%, 0.5 wt%, and 2 wt%) were loaded on the equimolar Al₂O₃–CeO₂ hybrid substrate (denoted as 0.25-Pt-Al-Ce, 0.5-Pt-Al-Ce, and 2-Pt-Al-Ce, respectively) and applied for the DRM process. All of the catalysts showed a stable DRM catalyzing performance, and the averaged DRM performances are listed and compared in

Table 2 DRM catalytic performance of Pt-Al-Ce catalysts with varied Pt loading amounts

Sample ID	H_2 production rate (mmol $g^{-1} h^{-1}$)	CO production rate (mmol $g^{-1} h^{-1}$)	H ₂ /CO ratio
Under dark con	ditions		
0.25-Pt-Al-Ce	225	337	0.67
0.20 1 0.111 00	225	33/	0.67
0.5-Pt-Al-Ce	446	528	0.85
Pt-Al-Ce	535	588	0.91
2-Pt-Al-Ce	682	685	0.99
Under solar irra	diation		
0.25-Pt-Al-Ce	313	424	0.74
0.5-Pt-Al-Ce	489	554	0.88
Pt-Al-Ce	657	666	0.99
2-Pt-Al-Ce	729	717	1.02

Table 2. It is clear that a higher Pt loading concentration is favorable in promoting the $\rm H_2$ and CO production rates as well as the $\rm H_2/CO$ ratio. However, by comparing Pt–Al–Ce with 2-Pt–Al–Ce, especially those under solar irradiation, the increase in the $\rm H_2/CO$ ratio is marginal when the Pt loading is over 1.0 wt%, despite the slight enhancement in $\rm H_2$ and CO production. Since Pt is a noble metal and expensive, by taking the cost of Pt into consideration, it is safe to reach the conclusion that 1.0 wt% Pt loading is optimal.

To further investigate the role of solar irradiation in the DRM process on Pt–Al–Ce catalysts, DRM performance tests at 650 °C and 600 °C under both dark and light conditions were conducted on Pt–Al–Ce catalysts, and the performance results of the test are listed along with the 700 °C data in Table S1.† The $\ln(r) - 1000/T$ correlations are plotted in Fig. 7 according to the Arrhenius equation based on the data listed in Table S1.† The $\ln(r) - 1000/T$ regression plots show a good linear correlation, and the linear regressions of the four datasets returned R^2 values close to 1.0, indicating accurate regression results. The apparent activation energy values are listed in Table 3 based on the calculated slopes of each regression curve.

As shown in Table 3, the apparent activation energy for $\rm H_2$ and CO production under dark conditions is 62.3 kJ mol⁻¹ and 41.9 kJ mol⁻¹, respectively. The apparent E_a of $\rm H_2$ and CO production under solar irradiation is 39.8 kJ mol⁻¹ and 27.8 kJ mol⁻¹, which are significantly lowered compared with those calculated under dark conditions, and similar observations on the reactant activation effect of light irradiation in the DRM process have also been documented by Yoshida *et al.*⁶⁵ and Miyauchi *et al.*^{66–68} It seems that the sunlight assisted in the activation of the reactants in the DRM process on Pt–Al–Ce catalysts. However, according to Fig. 6 and Table 1, $\rm H_2$ and CO production efficiency on Pt–Al is insensitive to light irradiation. Therefore, irradiation alone does not directly activate the reactants. Photoactive $\rm CeO_2$ seems to be the medium assisting the

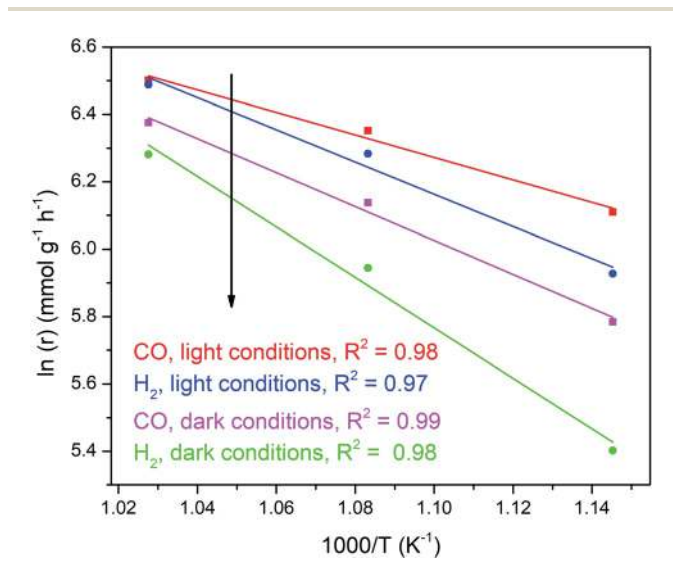


Fig. 7 Arrhenius $\ln(r)-1000/T$ plot for H $_2$ and CO gas production rates in the DRM process on Pt–Al–Ce catalysts under both dark and light conditions.

Table 3 The apparent activation energy of H_2 and CO production on Pt-Al-Ce under dark and light conditions

	Apparent $E_{\rm a}$ (kJ mol ⁻¹)		
Gas species	Dark	Light	
H_2	62.3	39.8	
H ₂ CO	41.9	27.8	

conversion of photon energy into chemical energy and facilitating the reaction. To determine the photoactivities of CeO₂ in Pt-Ce and Pt-Al-Ce, XPS deconvolution of Ce 3d of spent Pt-Ce and Pt-Al-Ce under both light and dark conditions under 700 °C was performed, and the results are shown in Fig. S10.† The light excitation can weaken the Ce-O bonds in CeO2 and lead to the generation of Ce^{3+} and oxygen vacancies ($Ce^{4+} + h\nu \rightarrow Ce^{3+} + h\nu \rightarrow Ce^{3+}$ V_O). 15,69 After the DRM reaction under the dark conditions, both Pt-Ce and Pt-Al-Ce exhibit lower molar ratios of Ce³⁺/(Ce³⁺ + Ce⁴⁺), valued at 17.4% and 15.6%, respectively, compared with fresh catalysts (fresh Pt-Ce: 24.3% and fresh Pt-Al-Ce: 24.7%) in Fig. 3, which is likely due to the oxidation of Ce³⁺ to Ce⁴⁺ by CO₂ in the DRM process. ^{15,69} In contrast, significantly higher molar ratios of Ce³⁺/(Ce³⁺ + Ce⁴⁺) on both catalysts were observed after the DRM reaction under the irradiation of concentrated sunlight (Pt-Ce: 39.1% and Pt-Al-Ce: 49.8%). This result suggests that the photoactive CeO₂ component in Pt-Ce and Pt-Al-Ce could contribute to the DRM performance under light irradiation through photocatalysis.

To further verify the role of photocatalysis in the photodriven DRM process on Pt–Al–Ce catalysts, a control experiment was conducted at 700 °C with a 530 nm long-pass filter. The cutoff photon energy of the 530 nm filter is 2.34 eV, which is slightly lower than the bandgap energy of Pt–Al–Ce (2.4 eV). Table 4 shows the comparison of 10 h average Pt–Al–Ce DRM performance under full-spectrum, 530 nm cut-off, and dark conditions. Under 530 nm cut-off conditions, where the photon energy is lower than the bandgap energy of Pt–Al–Ce, the DRM performance is almost the same as that under dark conditions. This result suggests that light irradiation enhances the DRM reaction through photocatalytic excitation of the catalyst, where photon energy is converted to chemical energy and leads to a significantly lower apparent activation energy for the production of $\rm H_2$ and $\rm CO$.

3.6 In situ DRIFTS analysis

To understand the effect of solar irradiation and investigate the intermediates involved in the photo-thermal driven DRM process, *in situ* DRIFTS analysis was conducted at various temperatures on Pt–Ce, Pt–Al–Ce, and Pt–Al under dark and light conditions in three gas environments: (1) DRM reaction gas (CO₂, and CH₄), (2) CO₂ only, and (3) CH₄ only.

As shown in Fig. 8, the exposure of DRM reaction gas to Pt–Ce and Pt–Al–Ce led to the generation of surface intermediates including formate (HCOO–), $^{70-72}$ bidentate carbonate (b-CO $_3^{2-}$), $^{72-75}$ and monodentate carbonate (m-CO $_3^{2-}$). 76,77 The peaks located at 1338 cm $^{-1}$ and 1308 cm $^{-1}$ were attributed to

Table 4 DRM catalytic performance of Pt-Al-Ce under varied light irradiation conditions at 700 $^{\circ}$ C

Reaction conditions	H_2 production rate (mmol $g^{-1} h^{-1}$)	CO production rate $(\text{mmol g}^{-1} \text{ h}^{-1})$
Full spectrum	657	666
>530 nm cut-off	531	593
Dark	535	588

gaseous $\mathrm{CH_4}$ (ref. 78) in the reactions. The doublet bands found at 2069 $\mathrm{cm^{-1}}$ and 1971 $\mathrm{cm^{-1}}$ were attributed to CO molecules linearly bonded to Pt atoms (Pt–CO). The CO molecules likely originated from $\mathrm{CO_2}$ reduction taking place on the catalyst surface. The absorption band located at 2069 $\mathrm{cm^{-1}}$ indicated the existence of linearly adsorbed CO on Pt, while the shoulder band centered at \sim 1971 $\mathrm{cm^{-1}}$ indicated the coverage of CO molecules on the boundary of Pt and the metal oxide support. On Pt–Al, only Pt–CO and bicarbonate bands were observed. Gaseous CO production was also observed as a duplet band at 2178 $\mathrm{cm^{-1}}$ and 2109 $\mathrm{cm^{-1}}$ at a temperature higher than 400 °C on Pt–Al.

Fig. 8a shows the surface intermediate behavior on Pt–Ce under a reaction gas atmosphere to temperature increase under dark conditions. All surface intermediates were found to show a decrease in absorption intensity due to the temperature increase. It seems that the formate intermediates are quite sensitive to temperature increases: the formate band intensity almost halved after the temperature increased from 200 °C to 600 °C. Only a small intensity decrease was found on m-CO $_3^{2-}$ and b-CO $_3^{2-}$. A red-shift effect was observed on the Pt–CO band as temperature increases, which was likely due to the decreased CO adsorption reducing the repulsion forces among CO molecules and leading to the red shift of the CO absorption band, sindicating CO desorption.

Fig. 8b shows the comparison between light and dark in situ DRIFTS results obtained on Pt-Ce. Under light irradiation, almost all of the surface intermediates showed a slight intensity decline. To rule out the thermal effect of the light irradiation, an IR thermometer was used to determine the temperature change of the sample in the in situ DRIFTS cell upon the light irradiation at room temperature. After \sim 5 min of sunlight irradiation, only a temperature rise of \sim 5 °C was observed on the catalyst surface. With such a minor temperature change at room temperature, the temperature change caused by the light irradiation may be negligible for tests conducted at 200-600 °C. The most noticeable change in the spectra is the sharp intensity decline of the formate band at ~1595 cm⁻¹ under light irradiation. The intensity of b-CO₃²⁻ was also found to decline under light irradiation. It seemed that m-CO₃²⁻ was relatively stable upon the light irradiation. Both formate and b- CO_3^{2-} have been viewed as important surface intermediates in CO generation in the DRM process. The intensity declines in the two surface intermediates suggest an accelerated rate of participation of the surface intermediates in the reaction process. 86 The activation

energy calculation chart shows that solar irradiation activates the surface intermediates and promotes the DRM reactions.

Similar surface intermediates were found on Pt-Al-Ce under dark conditions under a reaction gas atmosphere, as shown in Fig. 8c. Compared with Pt-Ce, the intensities of all of the carbonate absorption bands in the range of 1600-1200 cm⁻¹ were significantly weaker on Pt-Al-Ce, which was likely due to the lower concentration of CeO₂ in the Pt-Al-Ce material. Interestingly, the Pt-CO absorption band on Pt-Al-Ce was considerably stronger than that on Pt-Ce. In addition, the Pt-CO band on Pt-Al-Ce seemed to be less sensitive to temperature increase: only a small drop in the Pt-CO peak height was recorded while the temperature increased from 200 °C to 600 °C. The results indicate (1) a higher number of Pt nanoparticle active reaction sites, and (2) more reactive Pt nanoparticles on Pt-Al-Ce than those on Pt-Ce, which is likely promoted by the synergistic effects between Al₂O₃ and CeO₂ in the Pt-Al-Ce material. Similar to Pt-Ce, as the temperature rises, the intensity of absorption bands on Pt-Al-Ce declines. Similar to the observations on Pt-Ce, formate showed the most significant intensity decrease as the temperature increased, and b-CO₃²⁻ and m-CO₃²⁻ were also found to be sensitive to temperature increase. Similar to Pt-Ce, upon the concentrated solar irradiation, the formate and b-CO₃²⁻ intermediates showed a slight decrease in absorption band intensity, as shown in Fig. 8d, suggesting a promoted reaction rate in the DRM process.

Distinct from Pt–Ce and Pt–Al–Ce, only bicarbonate and Pt–CO were found on the surface of Pt–Al after coming into contact with the reaction gas. The intensity of the Pt–CO absorption band on Pt–Al was significantly weaker compared with Pt–Ce or Pt–Al–Ce, indicating fewer Pt nanoparticle active sites and less reactive Pt nanoparticles. The HCO_3^- intermediates seemed to be very sensitive to temperature increases. By increasing the temperature from 200 °C to 400 °C under dark conditions, the HCO_3^- absorption intensity decreased fast and disappears at 500 °C, as shown in Fig. 8e. Since DRM tests were conducted at high temperatures in this study, it is likely that bicarbonate is not an active intermediate in the DRM process. The low CO_2 affinity on Al_2O_3 might partially contribute to the poor DRM performance on Pt–Al.

To get a deeper understanding of the surface interaction between the catalysts and CO2 or CH4, in situ DRIFTS analyses were conducted under CO₂ and CH₄ atmospheres, respectively. The in situ DRIFTS results of Pt-Ce and Pt-Al-Ce obtained under a CO₂ atmosphere are shown in Fig. 9. Only weak Pt-CO bands were found on Pt-Al under the CO₂ atmosphere, and no carbonates bands were found, indicating low CO₂ affinity of the Pt-Al catalyst. The spectra obtained with Pt-Al are included in Fig. S11.† In Fig. 9, Pt–Ce and Pt–Al–Ce showed similar surface intermediates and DRIFTS spectra shapes when the two catalysts were exposed to CO2 gas. A formate band was found on both Pt-Ce and Pt-Al-Ce in the 1200-1400 cm⁻¹ range (Fig. 9ad),70 which was overshadowed by CH₄ gas in Fig. 8. Both formate bands were sensitive to temperature increase and concentrated solar irradiation, coinciding with the results observed under the DRM gas atmosphere. Similar to the observation made in Fig. 8,

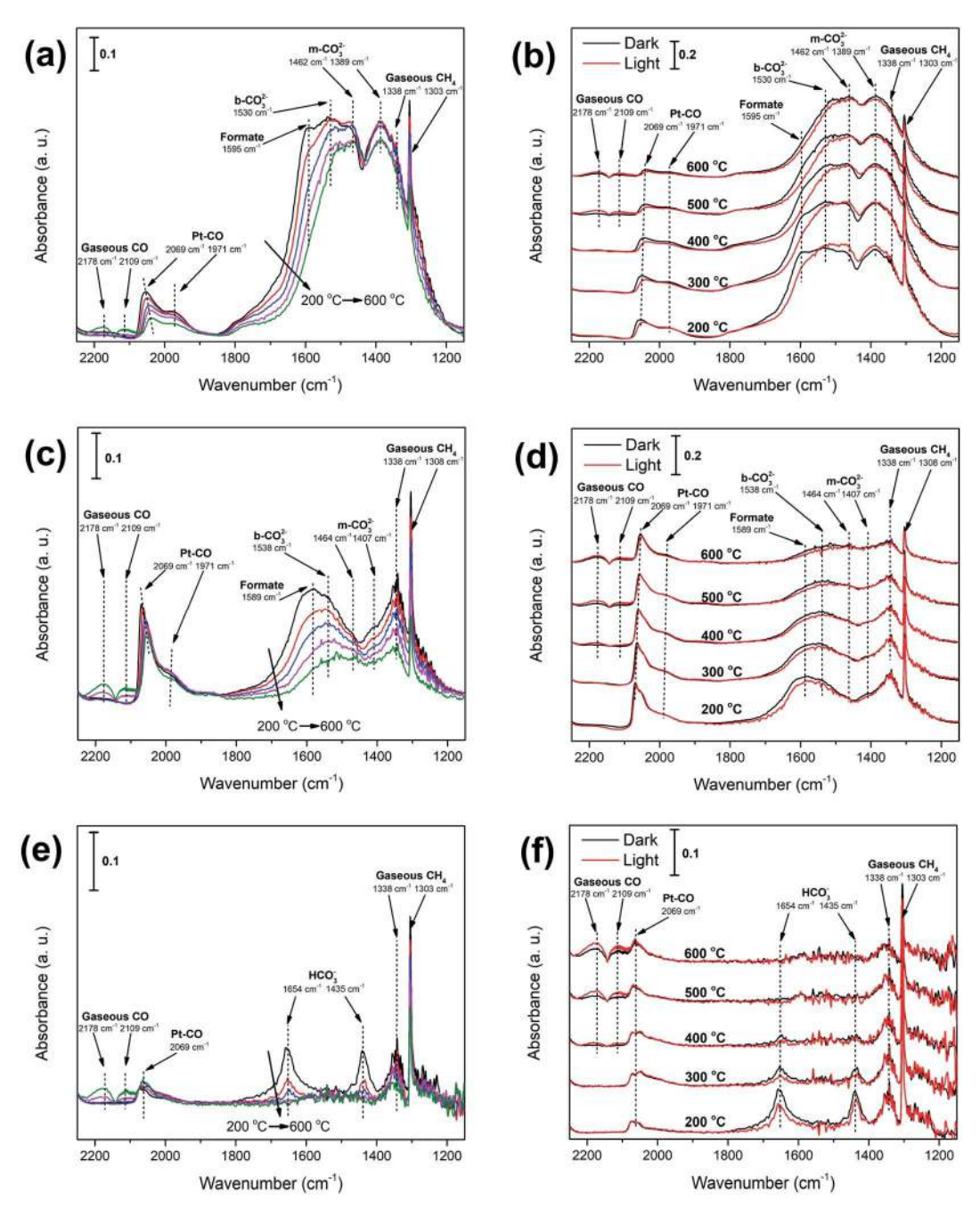


Fig. 8 In situ DRIFTS spectra under DRM reaction conditions in the dark on (a) Pt-Ce, (c) Pt-Al-Ce, and (e) Pt-Al, and dark-light comparison on (b) Pt-Ce, (d) Pt-Al-Ce, and (f) Pt-Al.

Pt-Al-Ce shows a stronger Pt-CO band, suggesting highly active and concentrated Pt nanoparticle reactions sites.

Under light irradiation, Pt–Ce shows formate absorption band intensity decline at all temperatures. At 200 °C and 300 °C, interestingly, it was found that the concentrated solar irradiation led to increases in m-CO $_3^{2-}$ and b-CO $_3^{2-}$ band intensity on Pt–Ce. The light irradiation likely caused oxygen vacancy generation on CeO $_2$ through a photocatalytic self-reduction process (CeO $_2$ + $hv \rightarrow$ CeO $_{2-x}$ + O $_2$),⁸⁷ which further promoted CO $_2$ adsorption and led to a slight intensity increase in m-CO $_3^{2-}$ and b-CO $_3^{2-}$ bands. At higher temperatures, all band intensities

of surface absorbed intermediates drop under light irradiation. Formate, m- $\mathrm{CO_3}^{2-}$, and b- $\mathrm{CO_3}^{2-}$ are active intermediates in $\mathrm{CO_2}$ reduction reactions. For the photo-induced band intensity decrease likely suggests the occurrence of $\mathrm{CO_2}$ reduction. However, gaseous CO bands were not observed in Fig. 9b, which is possibly due to the very low gaseous CO concentration on Pt–Ce. As shown in Fig. 9d, the light irradiation on Pt–Al–Ce resulted in considerable band intensity drops for the formate, m- $\mathrm{CO_3}^{2-}$, and b- $\mathrm{CO_3}^{2-}$ in the temperature range of 200–500 °C. A weak gaseous CO band was observed starting at 500 °C, confirming the occurrence of $\mathrm{CO_2}$ reduction reactions. The

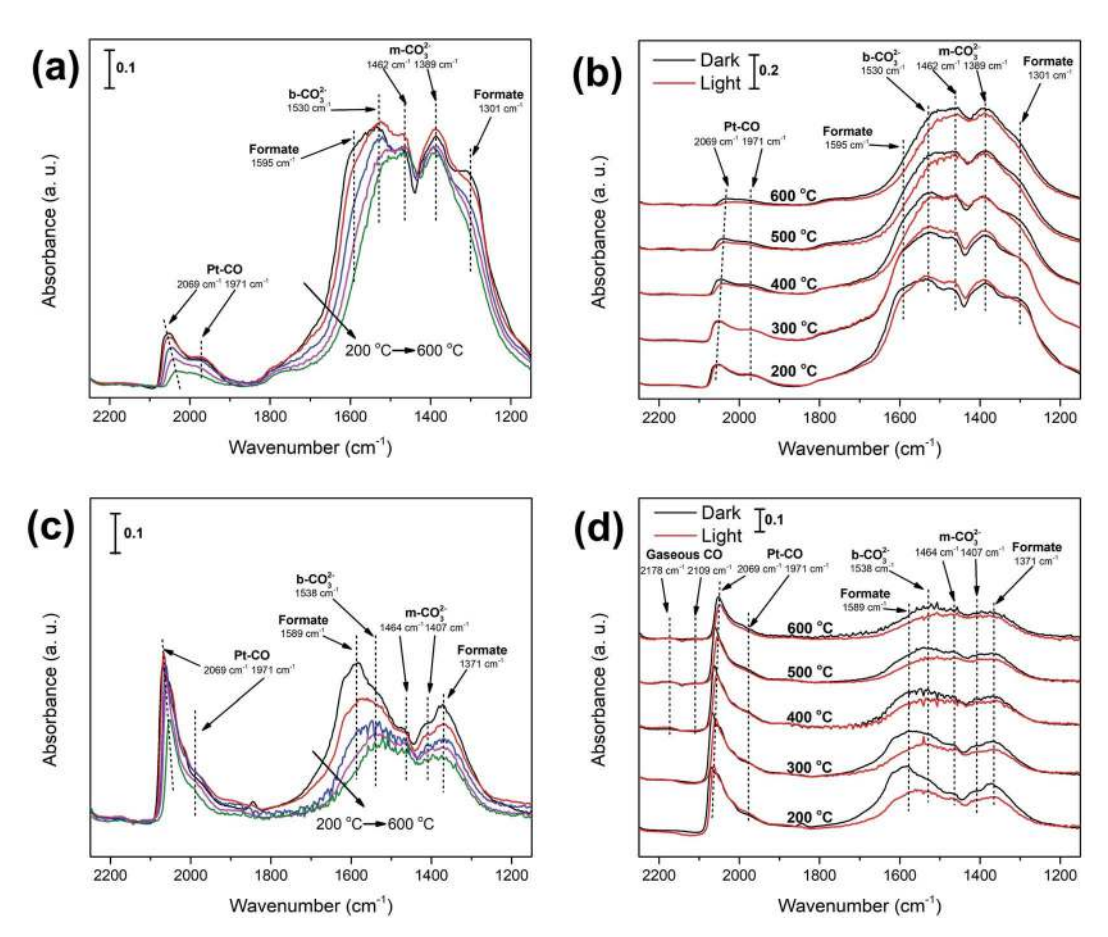


Fig. 9 In situ DRIFTS spectra under a CO_2 atmosphere in the dark on (a) Pt–Ce and (c) Pt–Al–Ce, and dark–light comparison on (b) Pt–Ce and (d) Pt–Al–Ce.

existence of a gaseous CO band with the Pt-Al-Ce catalyst suggests higher reactivity of Pt-Al-Ce compared to Pt-Ce.

The in situ DRIFTS results obtained under the CH₄ atmosphere are shown in Fig. 10, where spectra obtained in the 300-600 °C range are shown. For Pt-Ce, starting from 300 °C, strong carbonate bands were observed in the range of $1200-1600 \text{ cm}^{-1}$. The carbonates are likely the product of CH₄ oxidation by CeO₂. Weak Pt-CO bands were found. Compared with the Pt-CO bands observed under reaction gas and CO2 atmospheres, a significant redshift was detected: from 2069 cm⁻¹ under a CO₂-rich atmosphere to 2033 cm⁻¹ under a CH₄ atmosphere, indicating a low CO coverage on Pt nanoparticles. This observation is reasonable as only a trace amount of CH4 can be converted into CO on the Pt-Ce surface under a CH4 atmosphere. Formate was not found from the CH₄-DRIFTS results, which suggests that CO₂ is the source of formate intermediate generation. The intensities of the b-CO₃²⁻ bands observed under the CH₄ atmosphere were considerably lower than those found under the CO₂ or reaction gas atmosphere. This is likely because the conversion from m-CO₃²⁻ to b-CO₃²⁻ requires excessive CO₂ supply, which, however, was lacking under the CH₄ atmosphere. In addition, it does not seem that the surface intermediates are sensitive to concentrated solar irradiation under the CH₄ atmosphere, as compared in Fig. 10a and b. PtAl-Ce showed similar behavior as noticed on the Pt-Ce catalyst and similar surface intermediates were found (Fig. 10c and d). However, compared with Pt-Ce, Pt-Al-Ce showed a significantly stronger Pt-CO absorption band. The Pt-CO band on Pt-Al-Ce was evident even at a low temperature of 300 °C, which is a clear indicator of the occurrence of strong CH₄ oxidation. This result suggests that the Pt-Al-Ce material shows substantially higher surface reactivity compared to Pt-Ce. The DRIFTS data obtained on Pt-Al are included in Fig. S12.† No carbonate intermediates were found on Pt-Al, suggesting poor catalyst-CH₄ surface interaction. Surprisingly, however, a weak Pt-CO peak was found on Pt-Al under the CH₄ atmosphere. Without the presence of CO₂, the origin of Pt-CO can only be the oxidation of CH₄. It seems that Pt-Al is capable of dissociating trace amounts of CH₄ even at 300 °C. By combining the fact that Pt-CO was found on Pt-Al-Ce and Pt-Al under a CH₄ atmosphere, it seems that the existence of Al₂O₃ promotes the dissociation of CH₄, even at a relatively low temperature.

The observation that Pt nanoparticles on Pt–Al–Ce were more reactive and provided more reaction sites is well aligned with material characterization and the DRM catalytic performances. Firstly, the synergistic effects between Al₂O₃ and CeO₂ significantly promote the reactivity of Pt nanoparticles on Pt–Al–Ce. Secondly, since methane dissociation in the DRM process takes

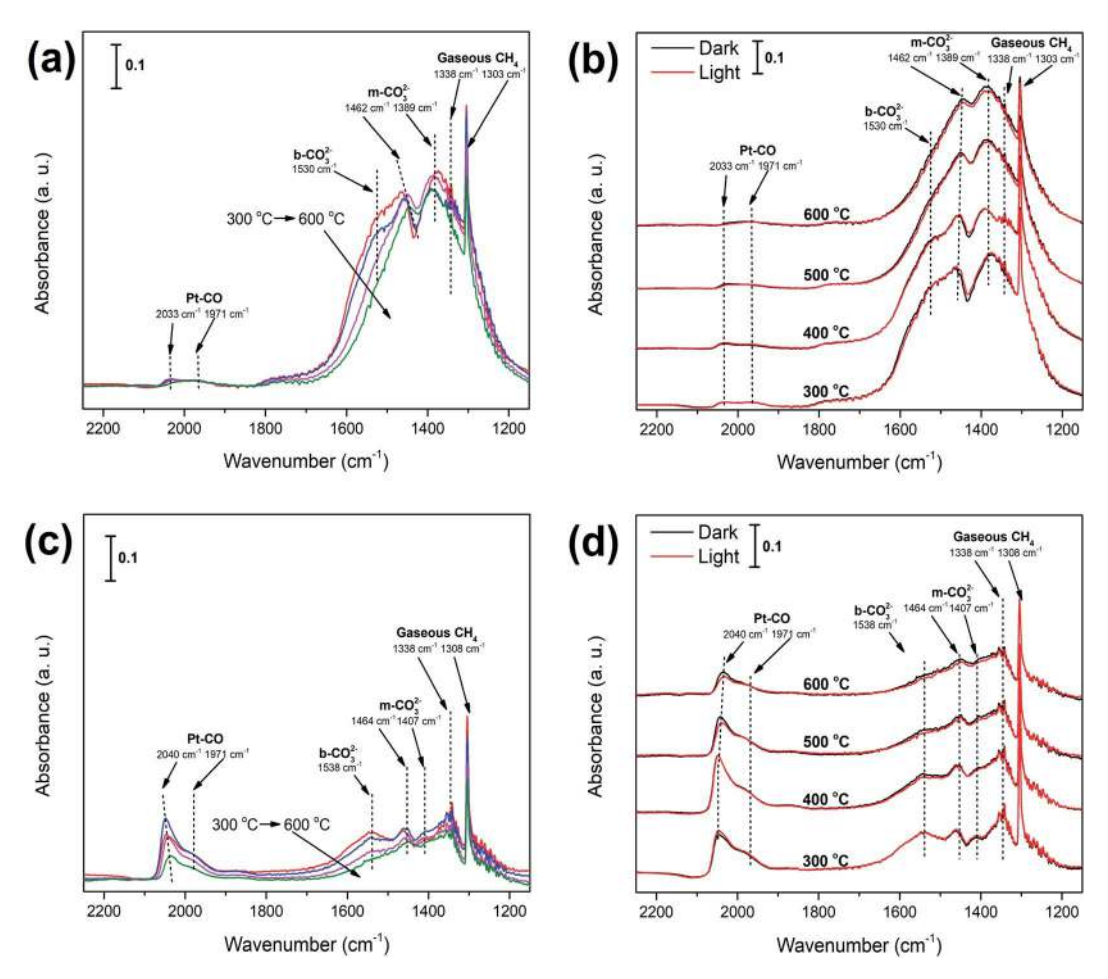


Fig. 10 In situ DRIFTS spectra under a CH₄ atmosphere in the dark on (a) Pt-Ce and (c) Pt-Al-Ce, and dark-light comparison on (b) Pt-Ce and (d) Pt-Al-Ce.

place on Pt nanoparticles,69 a higher reactivity in Pt nanoparticles suggests a promoted methane dissociation process on Pt-Al-Ce, which leads to an improved H₂ generation rate and a higher H₂/CO ratio in the produced gas.

3.7 Photo-thermal-driven DRM reaction mechanism on Pt-Al-Ce

Based on the experimental results and in situ DRIFTS analyses, a possible DRM reaction mechanism is proposed. CH₄ dissociation has been widely accepted to take place on Pt reaction sites forming C* and H* intermediates (reactions (1) and (2)), where Pt active sites activate methane and weaken the C-H bonding. 15,89 Two H* may couple and form H2 (reaction (3)). The reaction mechanism of CO₂ reduction to CO is slightly complicated. CO₂ can react with H* intermediates and form surface formate (reaction (6)), 89,90 which is converted into CO and -OH (reaction (7)). The formate intermediates may also react with H* and form CO and H2O through the RWGS mechanism (reaction (8)). CO can also be formed through the direct reduction of CO₂ by oxygen vacancies (V_O) on the catalyst surface (reaction (9)). Due to the high oxygen mobility properties of CeO₂, C* may be oxidized by CeO₂ lattice oxygen (O_L) and form CO (reaction (10)). Bidentate carbonate (b-CO₃²⁻) was also believed to be active in reacting with the C* intermediate and form CO (reaction (11)).91

The concentrated solar irradiation can additionally promote the DRM performance of Pt-Al-Ce catalysts through the photocatalytic effect. In the photocatalytic process, CeO2 is excited by photons and generate electrons (e⁻) and holes (h⁺) (reaction (12)). The electrons can reduce the bulk CeO₂ and generate V_O on the catalyst surface (reaction (13)), which enhances CO generation. As for methane dissociation, the photoexcited holes can extract H atoms from activated methane molecules on Pt nanoparticles,92 which facilitates the dissociation of CH_x* (reactions (14) and (15)) and leads to promoted H₂ production.

$$CH_4 \to CH_x^* + (4-x)H^*$$
 (1)

$$CH \to C^* + H^* \tag{2}$$

$$2H^* \to H_2 \tag{3}$$

$$CO_2 + O_L \rightarrow m - CO_3^{2-} \tag{4}$$

$$m-CO_3^{2-} \rightarrow b-CO_3^{2-}$$
 (under excessive CO_2) (5)

$$H^* + CO_2 \rightarrow HCOO-$$

$$HCOO- \rightarrow CO + -OH$$

(6)

(7)

$$H^* + HCOO \rightarrow CO + H_2O$$
 (8)

$$V_O + CO_2 \rightarrow CO + O_L$$
 (9)

$$C^* + O_L \rightarrow CO + V_O \tag{10}$$

$$b-CO_3^{2-} + C^* \rightarrow 2CO + O_L$$
 (11)

$$CeO_2 + h\nu \rightarrow CeO_2 + e^- + h^+ \tag{12}$$

$$Ce^{4+} + e^{-} \rightarrow Ce^{3+} + V_{O}$$
 (13)

$$CH_x^* + h^+ \rightarrow CH_{1-x}^* + H^*$$
 (14)

$$CH^* + h^+ \to C^* + H^*$$
 (15)

4. Conclusions

In this work, a Pt decorated Al_2O_3 – CeO_2 catalyst was prepared and applied for a photo-thermal driven DRM process. Strong synergistic effects were observed on the Pt–Al–Ce catalyst. Investigations revealed the bi-functional characteristics of the Al_2O_3 – CeO_2 binary substrate: Al_2O_3 stimulates CH_4 dissociation, while CeO_2 facilitates CO_2 reduction and coke elimination, leading to remarkable DRM catalyzing efficiency. The Pt–Al–Ce catalyst shows a near-unity H_2 /CO production ratio, which is likely related to the promoted reactivity and concentrated reaction sites of the Pt nanoparticles on the catalyst, as evidenced by *in situ* DRIFTS analyses. Concentrated solar irradiation of Pt–Al–Ce was found to facilitate reactant activation and reduce the reaction activation energy through the photocatalytic effect of the CeO_2 components, which leads to promoted DRM catalyzing efficiency.

Conflicts of interest

There are no conflicts to declare.

Acknowledgements

The authors gratefully acknowledge the financial supports from the U. S. National Science Foundation (Award #: CBET 1924466 and CBET 1924574). X. Feng is partially supported by the 2020 Graduate Summer Research Grant sponsored by J. Mike Walker '66 Department of Mechanical Engineering at Texas A&M University. The use of Material Characterization Facilities at Texas A&M University is acknowledged.

References

- 1 J. R. Rostrup-Nielsen, Catal. Today, 2002, 71, 243-247.
- 2 A. Iulianelli, S. Liguori, J. Wilcox and A. Basile, *Catal. Rev.*, 2016, **58**, 1–35.

- 3 A. Abdulrasheed, A. A. Jalil, Y. Gambo, M. Ibrahim, H. U. Hambali and M. Y. Shahul Hamid, *Renewable Sustainable Energy Rev.*, 2019, **108**, 175–193.
- 4 W.-J. Jang, J.-O. Shim, H.-M. Kim, S.-Y. Yoo and H.-S. Roh, *Catal. Today*, 2019, 324, 15–26.
- 5 Q. Jiang, S. Faraji, D. A. Slade and S. M. Stagg-Williams, in Membrane Science and Technology, ed. S. T. Oyama and S. M. Stagg-Williams, Elsevier, 2011, vol. 14, pp. 235–273.
- 6 H. Huang, M. Mao, Q. Zhang, Y. Li, J. Bai, Y. Yang, M. Zeng and X. Zhao, *Adv. Energy Mater.*, 2018, **8**, 1702472.
- 7 J. K. Adewole, A. L. Ahmad, S. Ismail and C. P. Leo, *Int. J. Greenhouse Gas Control*, 2013, 17, 46–65.
- 8 R. Franke, D. Selent and A. Börner, *Chem. Rev.*, 2012, **112**, 5675–5732.
- 9 Y. Zeng, X. Zhu, D. Mei, B. Ashford and X. Tu, Catal. Today, 2015, 256, 80–87.
- 10 J. Lu, C. Zhu, C. Pan, W. Lin, J. P. Lemmon, F. Chen, C. Li and K. Xie, *Sci. Adv.*, 2018, 4, eaar5100.
- 11 S. Shoji, A. S. Bin Mohd Najib, M.-W. Yu, T. Yamamoto, S. Yasuhara, A. Yamaguchi, X. Peng, S. Matsumura, S. Ishii, Y. Cho, T. Fujita, S. Ueda, K.-P. Chen, H. Abe and M. Miyauchi, *Chem Catalysis*, 2022, 2, 321–329.
- 12 S. Dasappa, H. V. Sridhar, G. Sridhar, P. J. Paul and H. S. Mukunda, *Biomass Bioenergy*, 2003, 25, 637–649.
- 13 M. Kushida, A. Yamaguchi, Y. Cho, T. Fujita, H. Abe and M. Miyauchi, *ChemPhotoChem*, 2021, 5, 275–281.
- 14 F. Pan, X. Xiang, W. Deng, H. Zhao, X. Feng and Y. Li, ChemCatChem, 2018, 10, 940–945.
- 15 F. Pan, X. Xiang, Z. Du, E. Sarnello, T. Li and Y. Li, *Appl. Catal.*, *B*, 2020, **260**, 118189.
- 16 R. Ma, S. Zhang, T. Wen, P. Gu, L. Li, G. Zhao, F. Niu, Q. Huang, Z. Tang and X. Wang, *Catal. Today*, 2019, 335, 20–30.
- 17 Y. Wang, J. Zhao, T. Wang, Y. Li, X. Li, J. Yin and C. Wang, *J. Catal.*, 2016, **337**, 293–302.
- 18 P. Li, X. Chen, Y. Li and J. W. Schwank, *Catal. Today*, 2019, 327, 90–115.
- 19 D. Pakhare and J. Spivey, *Chem. Soc. Rev.*, 2014, **43**, 7813-7837.
- 20 N. A. K. Aramouni, J. G. Touma, B. A. Tarboush, J. Zeaiter and M. N. Ahmad, *Renewable Sustainable Energy Rev.*, 2018, 82, 2570–2585.
- 21 P. Djinović, I. G. O. Črnivec, J. Batista, J. Levec and A. Pintar, *Chem. Eng. Process.: Process Intensif.*, 2011, **50**, 1054–1062.
- 22 C. Carrara, J. Múnera, E. A. Lombardo and L. M. Cornaglia, *Top. Catal.*, 2008, **51**, 98–106.
- 23 N. H. Elsayed, N. R. M. Roberts, B. Joseph and J. N. Kuhn, *Appl. Catal.*, *B*, 2015, **179**, 213–219.
- 24 D. Takami, A. Yamamoto and H. Yoshida, *Catal. Sci. Technol.*, 2020, **10**, 5811–5814.
- 25 C. Shi and P. Zhang, Appl. Catal., B, 2012, 115-116, 190-200.
- 26 P. G. Schulz, M. G. Gonzalez, C. E. Quincoces and C. E. Gigola, *Ind. Eng. Chem. Res.*, 2005, 44, 9020–9029.
- 27 S. Damyanova, B. Pawelec, K. Arishtirova, M. V. M. Huerta and J. L. G. Fierro, *Appl. Catal.*, *B*, 2009, **89**, 149–159.
- 28 F. Maleki and G. Pacchioni, *Top. Catal.*, 2020, **63**, 1717–1730.
- 29 I. Wysocka, J. Hupka and A. Rogala, Catalysts, 2019, 9, 540.

- 30 R. Tang, Z. Zhu, C. Li, M. Xiao, Z. Wu, D. Zhang, C. Zhang, Y. Xiao, M. Chu, A. Genest, G. Rupprechter, L. Zhang, X. Zhang and L. He, ACS Mater. Lett., 2021, 3, 1652–1659.
- 31 R. Benrabaa, A. Löfberg, J. Guerrero Caballero, E. Bordes-Richard, A. Rubbens, R.-N. Vannier, H. Boukhlouf and A. Barama, *Catal. Commun.*, 2015, **58**, 127–131.
- 32 H. U. Hambali, A. A. Jalil, A. A. Abdulrasheed, T. J. Siang, T. A. T. Abdullah, A. Ahmad and D.-V. N. Vo, *Int. J. Energy Res.*, 2020, 44, 5696–5712.
- 33 H. Pines and W. O. Haag, J. Am. Chem. Soc., 1960, 82, 2471–2483.
- 34 D. Zhang, J. Zhang and D. Sun, *Appl. Catal.*, *A*, 2020, **606**, 117800.
- 35 T. Li, L. Zhang, Z. Tao, C. Hu, C. Zhao, F. Yi, X. Gao, X. Wen, Y. Yang and Y. Li, *Fuel*, 2020, **279**, 118487.
- 36 S. Wu, Y. Li, Q. Zhang, Z. Jiang, Y. Yang, J. Wu and X. Zhao, *Energy Environ. Sci.*, 2019, **12**, 2581–2590.
- 37 S. Wu, Y. Li, Q. Zhang, Q. Hu, J. Wu, C. Zhou and X. Zhao, *Adv. Energy Mater.*, 2020, **10**, 2002602.
- 38 H. Liu, X. Meng, T. D. Dao, H. Zhang, P. Li, K. Chang, T. Wang, M. Li, T. Nagao and J. Ye, *Angew. Chem., Int. Ed.*, 2015, 54, 11545–11549.
- 39 H. Liu, T. D. Dao, L. Liu, X. Meng, T. Nagao and J. Ye, Appl. Catal., B, 2017, 209, 183–189.
- 40 G. Zhang, S. Wu, Y. Li and Q. Zhang, *Appl. Catal.*, *B*, 2020, **264**, 118544.
- 41 M. Mao, Q. Zhang, Y. Yang, Y. Li, H. Huang, Z. Jiang, Q. Hu and X. Zhao, *Green Chem.*, 2018, **20**, 2857–2869.
- 42 L. Liu, H. Zhao, J. M. Andino and Y. Li, ACS Catal., 2012, 2, 1817–1828.
- 43 B. M. Reddy, K. N. Rao, G. K. Reddy, A. Khan and S.-E. Park, J. Phys. Chem. C, 2007, 111, 18751–18758.
- 44 S. Boullosa-Eiras, E. Vanhaecke, T. Zhao, D. Chen and A. Holmen, *Catal. Today*, 2011, **166**, 10–17.
- 45 L. S. F. Feio, C. E. Hori, S. Damyanova, F. B. Noronha, W. H. Cassinelli, C. M. P. Marques and J. M. C. Bueno, Appl. Catal., A, 2007, 316, 107–116.
- 46 Z. Li and K. Sibudjing, ChemCatChem, 2018, 10, 2994-3001.
- 47 C. Anandan and P. Bera, Appl. Surf. Sci., 2013, 283, 297–303.
- 48 C. Lv, C. Zhu, C. Wang, D. Li, X. Ma and D. Yang, *AIP Adv.*, 2015, 5, 037107.
- 49 R. Murugan, G. Ravi, G. Vijayaprasath, S. Rajendran, M. Thaiyan, M. Nallappan, M. Gopalan and Y. Hayakawa, *Phys. Chem. Chem. Phys.*, 2017, **19**, 4396–4404.
- 50 K. Wang, Y. Chang, L. Lv and Y. Long, *Appl. Surf. Sci.*, 2015, **351**, 164–168.
- 51 M. Li, X. Pan, M. Jiang, Y. Zhang, Y. Tang and G. Fu, *Chem. Eng. J.*, 2020, **395**, 125160.
- 52 P. M. A. Sherwood, Surf. Sci. Spectra, 1998, 5, 1-3.
- 53 J. van den Brand, W. G. Sloof, H. Terryn and J. H. W. de Wit, Surf. Interface Anal., 2004, 36, 81–88.
- 54 M. Yang, G. Shen, Q. Wang, K. Deng, M. Liu, Y. Chen, Y. Gong and Z. Wang, *Molecules*, 2021, 26, 6363.
- 55 A. Elaziouti, N. Laouedj, A. Bekka and R.-N. Vannier, *J. King Saud Univ.*, *Sci.*, 2015, 27, 120–135.
- 56 R. Singh and R. K. Soni, Appl. Phys. A, 2014, 116, 689-701.

- 57 P. Makuła, M. Pacia and W. Macyk, J. Phys. Chem. Lett., 2018, 9, 6814–6817.
- 58 L. Tao, Y. Shi, Y.-C. Huang, R. Chen, Y. Zhang, J. Huo, Y. Zou, G. Yu, J. Luo, C.-L. Dong and S. Wang, *Nano Energy*, 2018, 53, 604–612.
- 59 B. Choudhury, P. Chetri and A. Choudhury, *J. Exp. Nanosci.*, 2015, 10, 103–114.
- 60 M. Alabdullah, M. Ibrahim, D. Dhawale, J. A. Bau, A. Harale, S. Katikaneni and J. Gascon, *ChemCatChem*, 2021, 13, 2879– 2886.
- 61 M. Usman, W. M. A. Wan Daud and H. F. Abbas, *Renewable Sustainable Energy Rev.*, 2015, 45, 710–744.
- 62 T. Wang, F. Jiang, G. Liu, L. Zeng, Z.-j. Zhao and J. Gong, *AIChE J.*, 2016, **62**, 4365–4376.
- 63 A. Arslan and T. Doğu, Int. J. Hydrogen Energy, 2016, 41, 16752-16761.
- 64 K. Tomishige, T. Kimura, J. Nishikawa, T. Miyazawa and K. Kunimori, *Catal. Commun.*, 2007, **8**, 1074–1079.
- 65 L. Yuliati, H. Itoh and H. Yoshida, *Chem. Phys. Lett.*, 2008, 452, 178–182.
- 66 S. Shoji, X. Peng, A. Yamaguchi, R. Watanabe, C. Fukuhara, Y. Cho, T. Yamamoto, S. Matsumura, M.-W. Yu, S. Ishii, T. Fujita, H. Abe and M. Miyauchi, *Nat. Catal.*, 2020, 3, 148–153.
- 67 Y. Cho, A. Yamaguchi and M. Miyauchi, *Catalysts*, 2021, 11, 18
- 68 Y. Cho, S. Shoji, A. Yamaguchi, T. Hoshina, T. Fujita, H. Abe and M. Miyauchi, *Chem. Commun.*, 2020, 56, 4611–4614.
- 69 Z. Du, F. Pan, E. Sarnello, X. Feng, Y. Gang, T. Li and Y. Li, *J. Phys. Chem. C*, 2021, **125**, 18684–18692.
- 70 D. G. Araiza, A. Gómez-Cortés and G. Díaz, *Catal. Sci. Technol.*, 2017, 7, 5224–5235.
- 71 G. Jacobs, U. M. Graham, E. Chenu, P. M. Patterson, A. Dozier and B. H. Davis, *J. Catal.*, 2005, **229**, 499–512.
- 72 L. F. Bobadilla, J. L. Santos, S. Ivanova, J. A. Odriozola and A. Urakawa, *ACS Catal.*, 2018, **8**, 7455–7467.
- 73 I. Tankov, W. H. Cassinelli, J. M. C. Bueno, K. Arishtirova and S. Damyanova, *Appl. Surf. Sci.*, 2012, **259**, 831–839.
- 74 A. Yee, S. J. Morrison and H. Idriss, *J. Catal.*, 1999, **186**, 279–295.
- 75 Z. Hou, X. Zhou, T. Lin, Y. Chen, X. Lai, J. Feng and M. Sun, New J. Chem., 2019, 43, 5719–5726.
- 76 L. Liu, C. Zhao, J. Xu and Y. Li, *Appl. Catal.*, *B*, 2015, **179**, 489–499.
- 77 F. Zhao, Z. Liu, W. Xu, S. Yao, A. Kubacka, A. C. Johnston-Peck, S. D. Senanayake, A.-Q. Zhang, E. A. Stach, M. Fernández-García and J. A. Rodriguez, *J. Phys. Chem. C*, 2014, 118, 2528–2538.
- 78 NIST Chemistry WebBook, NIST Standard Reference Database Number 69, ed., P. J. Linstrom and W. G. Mallard, National Institute of Standards and Technology, Gaithersburg MD, 2020, p. 20899.
- 79 O. Pozdnyakova-Tellinger, D. Teschner, J. Kröhnert, F. C. Jentoft, A. Knop-Gericke, R. Schlögl and A. Wootsch, J. Phys. Chem. C, 2007, 111, 5426–5431.
- 80 M. J. Kappers, J. T. Miller and D. C. Koningsberger, *J. Phys. Chem.*, 1996, **100**, 3227–3236.

- 81 O. Pozdnyakova, D. Teschner, A. Wootsch, J. Kröhnert, B. Steinhauer, H. Sauer, L. Toth, F. C. Jentoft, A. Knop-Gericke, Z. Paál and R. Schlögl, *J. Catal.*, 2006, 237, 1–16.
- 82 G. Jacobs, L. Williams, U. Graham, D. Sparks and B. H. Davis, *J. Phys. Chem. B*, 2003, **107**, 10398–10404.
- 83 C. Morterra, A. Zecchina, S. Coluccia and A. Chiorino, *J. Chem. Soc., Faraday Trans.* 1, 1977, 73, 1544–1560.
- 84 J. Szanyi and J. H. Kwak, *Phys. Chem. Chem. Phys.*, 2014, **16**, 15117–15125.
- 85 A. Kaftan, M. Kusche, M. Laurin, P. Wasserscheid and J. Libuda, *Appl. Catal.*, *B*, 2017, **201**, 169–181.
- 86 L. Liu, Y. Jiang, H. Zhao, J. Chen, J. Cheng, K. Yang and Y. Li, *ACS Catal.*, 2016, **6**, 1097–1108.

- 87 H. R. Park, A. U. Pawar, U. Pal, T. Zhang and Y. S. Kang, *Nano Energy*, 2021, **79**, 105483.
- 88 W. Bi, Y. Hu, N. Jiang, L. Zhang, H. Jiang, X. Zhao, C. Wang and C. Li, *Appl. Catal.*, *B*, 2020, **269**, 118810.
- 89 J. Niu, X. Du, J. Ran and R. Wang, *Appl. Surf. Sci.*, 2016, 376, 79–90.
- 90 X. Su, X. Yang, B. Zhao and Y. Huang, *J. Energy Chem.*, 2017, **26**, 854–867.
- 91 X. Li, Z.-J. Zhao, L. Zeng, J. Zhao, H. Tian, S. Chen, K. Li, S. Sang and J. Gong, *Chem. Sci.*, 2018, **9**, 3426–3437.
- 92 Q. Li, Y. Ouyang, H. Li, L. Wang and J. Zeng, *Angew. Chem., Int. Ed.*, 2021, **61**, e202108069.